Chemical Science

ROYAL SOCIETY OF CHEMISTRY

EDGE ARTICLE

View Article Online
View Journal | View Issue

Cite this: *Chem. Sci.*, 2025, **16**, 1432

All publication charges for this article have been paid for by the Royal Society of Chemistry

Received 12th September 2024
Accepted 11th December 2024

DOI: 10.1039/d4sc06172a

rsc.li/chemical-science

Determinants of regioselectivity of heterostructures in cation exchange reactions†

Xuelian Qu,‡[a] Huisheng Zhang,‡[b] Tianyi Gao,[a] Fei Zhang,[a] Ying Zhang,[a] Ding-Jiang Xue[cd] and Yang Liu*[a]

A cation exchange (CE) reaction offers a remarkable opportunity to create versatile metal sulfide nanocrystals (NCs) with arbitrary complexity in composition, structure, and functionality. The concept of regioselectivity has been discovered and developed to build the target heterostructures through CE reactions, yet a general principle of regioselectivity remains unclear. In this work, we establish connections between experimental results and theoretical insights to elucidate the determinants of regioselectivity using designed aliovalent CE reactions on a two-dimensional template. Our findings demonstrate that the local density of delocalized electrons between the host lattice and guest cations determines the reaction heat on different facets, thereby dictating the resulting structure of the nanoplates after CE reactions. We unravel the mechanism of CE reactions occurring primarily at the edges of the nanoplates and manipulate the occurrence of these reactions by employing active or passivated edges. Consequently, a series of heterostructures with distinct combinations of metal sulfide phases can be synthesized by manipulating these determinants. Our work paves the way for the synthesis of copper sulfide-based heterostructures with multifunctionalities and emergent properties.

Introduction

CE reactions have emerged as a powerful chemical method for synthesizing novel NCs with diverse applications including photovoltaics, photonics, energy storage, (photo)electrocatalysis, and magnetic devices.[1–8] In the realm of copper sulfide-based nanomaterials, CE plays a particularly crucial role in the synthesis of multinary homogeneous and heterogeneous NCs, leveraging the unique template of $Cu_{2-x}S$.[9–12] The template offers a unique host lattice that allows controllable uptake of foreign cations under desired reaction conditions.[13–15] Typically, CE of the hexagonal close-packed (hcp) template of $Cu_{2-x}S$ yields NCs with an hcp-type product structure, preserving the sulfur sublattices despite the hcp phase's thermodynamic metastability in certain metal sulfide NCs.[16,17] Regioselectivity in CE reactions describes the precise modification of targeted locations on the template NCs by incoming cations.[18–21] For example, Schaak and colleagues observed 113 individual heterostructured nanostructures and predicted the existence of 65 520 distinct multicomponent metal sulfide heterostructures through regioselective CE reactions.[15] Millstone's group demonstrated the controlled synthesis of homogeneous or heterogeneous NCs by selectively depositing incoming cations.[22,23]

While regioselectivity offers programmable synthesis of metal sulfide NCs with desired compositions and structures, its underlying mechanism remains obscure. Specifically, the incoming cations tend to replace the Cu atoms at the vertex (corner) and/or edges on anisotropic $Cu_{2-x}S$ templates (such as plates and rods).[13,15,24] However, theoretical and experimental studies have provided limited insights into this regioselectivity. Furthermore, predicting the outcomes of CE reactions becomes even more challenging when foreign cations are incorporated into heterostructures. Therefore, establishing an experimental–theoretical connection to unravel the mechanism of regioselectivity in CE reactions would greatly facilitate the discovery of a diverse library of functional metal sulfide NCs and heterostructures.

In this work, we systematically investigated the regioselectivity of CE reactions on $Cu_{2-x}S$ and its heterostructures. We focused on three representative heterocations, namely Zn, Cd, and In, which possess stable valence, moderate reactivity, and a strong affinity for sulfur.[13,15,25] Similar reaction mechanisms are expected for other divalent and trivalent cations. DFT

[a]Department of Materials Science, Fudan University, Shanghai 200433, China. E-mail: liuyang_fd@fudan.edu.cn

[b]Research Institute of Materials Science of Shanxi Normal University & Key Laboratory of Magnetic Molecules and Magnetic Information Materials of Ministry of Education, Taiyuan 030031, China

[c]Beijing National Laboratory for Molecular Sciences (BNLMS), CAS Key Laboratory of Molecular Nanostructure and Nanotechnology, Institute of Chemistry, Chinese Academy of Sciences, Beijing 100190, China

[d]University of Chinese Academy of Sciences, Beijing 100049, China

† Electronic supplementary information (ESI) available. See DOI: https://doi.org/10.1039/d4sc06172a

‡ These authors contributed equally.

calculations revealed that the CE reactions generally prefer to take place on the edges of the nanoplates. However, the regioselectivity varied depending on the guest cations and host lattices, influenced by the density of delocalized electrons. Guided by theoretical calculations, we synthesized a diverse collection of copper sulfide-based heterostructures by adjusting the template, foreign cations, and reaction temperatures. Notably, at mild reaction temperatures, the observed regioselectivity of CE reactions aligned well with the theoretical predictions. However, as the reaction temperature increased, this selectivity became less pronounced. The fundamental insights gained from this work provide valuable guidance for engineering solid-state CE reactions, enabling the creation of functional metal sulfide nanomaterials with atomic precision.

Results and discussion

Theoretical understanding for the regioselectivity in CE reactions

We chose roxbyite $Cu_{1.81}S$ as the template to study CE reactions as its disordered hcp-type anionic framework (Fig. S1–S3†). $Cu_{1.81}S$ naturally adopts a hexagonal plate-like morphology, exposing basal and edge planes that correspond to the (800) and (080) crystal planes in the $Cu_{1.81}S$ unit cell, respectively. In line with previous reports, we acknowledge that trivalent cations (M^{3+}) can coexist with Cu^+ in $Cu_{2-x}S$ unit cells by substituting triple Cu^+ ions to maintain charge balance, producing $Cu_{2-x}S$/$CuMS_2$ heterostructures.[24,26–28] By contrast, such partial CE is not observed for divalent cations (M^{2+}), as they tend to replace all Cu^+ ions in a $Cu_{2-x}S$ unit cell in a 1 : 2 ratio for electroneutrality, leading to the formation of $Cu_{2-x}S$/MS heterostructures.[13,16,27] To gain a thermodynamic understanding of the regioselectivity for $Cu_{1.81}S$ nanoplates, we calculated the heat of reaction (Δ_rE), which is of pivotal importance for determining the feasibility of the CE reaction (see the Materials and methods and the ESI† for details). Δ_rE is defined as the difference in total energy between the compound and the total energies of its constituent elements *via* DFT calculations.[24,29] Here, Cu atoms were replaced by a foreign atom (Zn, Cd, and In) on either basal (800) or (080) edge planes. A negative value of Δ_rE indicates that cationic substitution is energetically favorable on the surface. Additionally, we calculated Δ_rE for CE reactions on other heterostructure counterparts, including $CuInS_2$, ZnS, and CdS to further reveal the regioselectivity on the heterostructures. The DFT-based Δ_rE values (Table S1†) are plotted in Fig. 1, and the relaxed structural models are provided in Fig. S4–S6.† Notably, the DFT calculations in this work only consider electronic energies at 0 K. The initial stage of the CE process could also increase the entropy of the lattices, providing an additional driving force.

As shown in Fig. 1a, the CE reactions on $Cu_{1.81}S$, $CuInS_2$, ZnS and CdS are thermodynamically favorable, as indicated by the negative values of the Δ_rE values. Interestingly, all CE reactions exhibit a preference for the edges ($\Delta_rE_{edge} < \Delta_rE_{basal} < 0$). Among these reactions, the incorporation of In into $Cu_{1.81}S$ (denoted as $In \rightarrow Cu_{1.81}S$) displays the most negative Δ_rE_{edge}, while the $Zn \rightarrow CuInS_2$ reaction exhibits the maximal energy difference between two surfaces (ΔE, defined as $|\Delta_rE_{edge} - \Delta_rE_{basal}|$). These observations suggest that the $In \rightarrow Cu_{1.81}S$ and $Zn \rightarrow CuInS_2$ reactions are predicted to have the highest regioselectivity, favoring their occurrence on the edges. Conversely, the ΔE value for the $Zn \rightarrow Cu_{1.81}S$ reaction is minimal, indicating indiscriminate CE reactions of Zn^{2+} on both types of surfaces of $Cu_{1.81}S$.

We further performed electron localization function (ELF) calculations of the (001) and (100) surfaces of $CuInS_2$, CdS and ZnS to elucidate the origin of the different Δ_rE (Fig. 1b–e and S7†). The ELF essentially quantifies the local Pauli repulsion among electrons.[30,31] We also recorded the calculated ELF values in Table S2.† After the CE reaction, an increased charge density overlap between sulfur and foreign cations is observed,

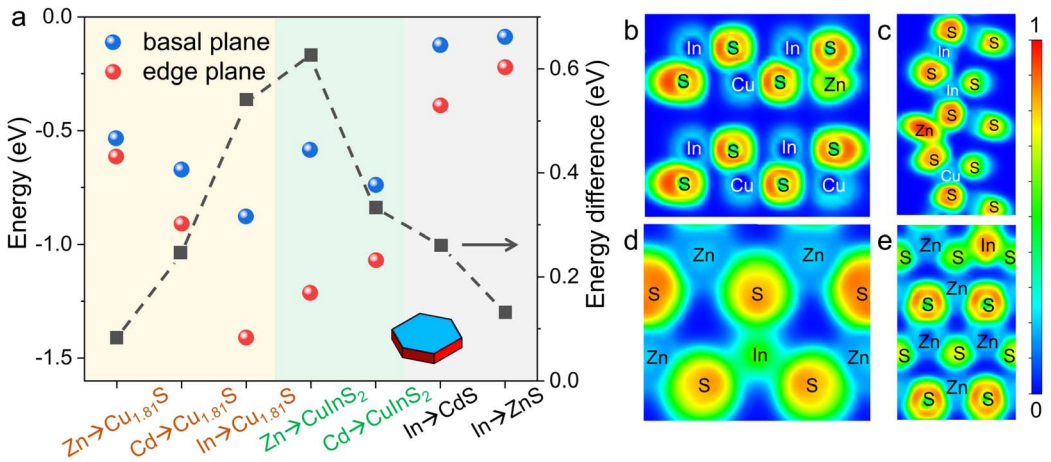

Fig. 1 Heat of reaction and energy difference of CE reactions. (a) Plot of Δ_rE values of CE reactions on the basal and edge planes of template nanoplates. The ΔE values between the basal and edge planes of different reactions were plotted in black squares. For reading convenience, we colored the plot according to the different metal sulfide templates. (b and c) Sliced electron localization function (ELF) of the $Zn \rightarrow CuInS_2$ reaction on the (001) and (100) planes of $CuInS_2$, respectively. (d and e) Sliced ELF of the $In \rightarrow ZnS$ reaction on the (001) and (100) planes of ZnS, respectively.

which can be attributed to the higher density of delocalized electrons.[32,33] The strongly localized electron clouds signify strong interactions between cations and surrounding anions.[9,34] Thus, a higher ELF value indicates the formation of stronger interactions between the cation and the surrounding sulfur ions. This explains the negative value of $\Delta_r E$ for all proposed CE reactions, as shown in Fig. 1a. Furthermore, the higher ELF value of the Zn atom at the edge ($n = 0.96$) compared to that on the basal plane ($n = 0.47$) of $CuInS_2$ aligns with the DFT calculations favoring the Zn → $CuInS_2$ reaction at the edges. The difference between the ELF values of Zn atoms on the two surfaces of the Zn → $CuInS_2$ reaction is larger than that of the In atoms on the two surfaces of the In → ZnS reaction. This supports the higher regioselectivity ($\Delta E = 0.626$ eV) of the Zn → $CuInS_2$ reaction compared to the In → ZnS reaction ($\Delta E = 0.261$ eV). The trend of ELF values ($n_{edge} > n_{basal}$) on the two types of surfaces can be extended to other reactions, with less favored reactions (*e.g.*, In → CdS) exhibiting lower ELF values of the foreign atoms ($n_{In} = 0.37$) and favored reactions (*e.g.*, Cd → $CuInS_2$) showing the higher ELF values of the foreign atoms ($n_{Cd} = 0.77$).

Regioselectivity of CE reactions on a copper sulfide template

We chose $Cu_{1.81}S$ nanoplates as the template to evaluate the theoretical prediction of the regioselectivity of CE reactions on $Cu_{1.81}S$ as its two-dimensional morphology only exposes (100) and (010) groups of facets on basal and edge planes, respectively. Structural analyses including transmission electron microscopy (TEM) images, high-resolution TEM (HRTEM) images, fast Fourier transformation (FFT) patterns and powder X-ray diffraction (XRD) patterns of the template $Cu_{1.81}S$ nanoplates are provided in Fig. S8.† To carefully examine the cation diffusion pathway and the outcome of partial CE reactions, a mild heating temperature of 55 °C was used. As shown in Fig. 2a–c, we obtained heteronanoplates with (1) fully covered edges ($Cu_{1.81}S$@$CuInS_2$), (2) vertex-covered edges ($Cu_{1.81}S$/CdS), and (3) open edges ($Cu_{1.81}S$/ZnS) after In^{3+}, Cd^{2+}, and Zn^{2+} exchange, respectively. Microscopic analysis in Fig. 2d–f reveals clear heterointerfaces in these heterostructures.

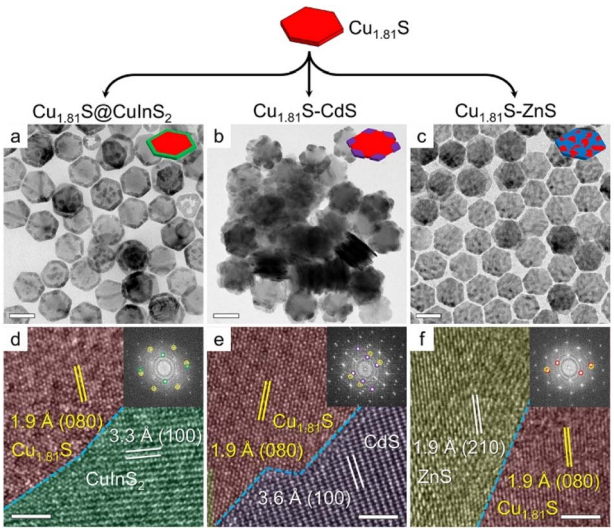

Fig. 2 CE reactions on $Cu_{1.81}S$ nanoplates. TEM and HRTEM images of different CE reaction products obtained through (a and d) In^{3+}, (b and e) Cd^{2+}, and (c and f) Zn^{2+} exchange, respectively. For convenience, HRTEM images are colored according to different metal sulfide domains. The colors correspond to the circles in the FFT patterns of the insets. Scale bars: (a–c) 100 nm; (d–f) 2 nm.

Consistent with the DFT predictions, the highest regioselectivity ($\Delta E = 0.626$ eV) observed in the In^{3+} exchange reaction allows In^{3+} to replace Cu atoms specifically from the edges of the nanoplates, producing $Cu_{1.81}S$@$CuInS_2$ heterostructures. By contrast, the minimal $\Delta E = 0.084$ eV of Zn^{2+} exchange indicates indiscriminate CE reactions on both basal and edge planes of the nanoplates. Cd^{2+} exchange exhibits a moderate selectivity ($\Delta E = 0.245$ eV) and guides the CE reactions to occur from the edges, but its larger cation radius (Cd^{2+}: 78 pm, Cu^{+}: 60 pm, Zn^{2+}: 60 pm, and In^{3+}: 62 pm)[35,36] drives the reaction to localize on the six sterically open vertices (Fig. S9†). The hexagonal morphology of the nanoplates was preserved after the CE reaction owing to the similar unit cells between the template and product nanoplates, where their sulfur sublattices share the same hcp-type arrangement with a ≤7.2% lattice expansion/shrinkage (calculations of lattice mismatch are provided in Table S3†). The minor lattice mismatch between $Cu_{1.81}S$ and other metal sulfide unit cells allowed the CE reactions to occur with minimal change to the anionic framework.

Regioselectivity of CE reactions on $Cu_{1.81}S$@$CuInS_2$ heterostructures

We further examined the CE reactions on the above heterostructures from both experimental and theoretical perspectives. We discovered that both the structure of the templates and the reaction temperature strongly influence the regioselectivity of the CE reactions. As shown in Fig. 3, the hexagonal core@shell template nanoplates were preserved after the CE reactions, indicating that the guest cations adopt the pristine coordination environments in the host lattice without modifying the crystal structure of the template. Consistent with the DFT results, Zn^{2+} incorporated into $Cu_{1.81}S$@$CuInS_2$ from the edges, resulting in $Cu_{1.81}S$@$(CuIn)_{0.96}Zn_{0.04}S_2$ heterostructures. The immiscible heterointerface between the two domains was clearly observed in the high-angle annular dark field scanning TEM (HAADF-STEM) image (Fig. 3b). Quantitative STEM energy dispersive X-ray spectroscopy (STEM-EDS) results for this and the following samples are provided in Fig. S10 in the ESI.† Elemental maps of sulfur in Fig. S11a† show that sulfur is distributed throughout the entire nanoplate. For convenience, sulfur elemental maps of individual nanoplates are shown in Fig. S11.† The incorporation of Zn^{2+} on the $CuInS_2$ edges is also supported by elemental maps (Fig. 3e and S12a†) and a 0.15° shift in XRD patterns (Fig. S13†). Because the Zn → $CuInS_2$ reaction has more negative reaction energy compared to that of the Zn → $Cu_{1.81}S$ reaction, the $CuInS_2$ shell appears to be a barrier that hinders the diffusion of Zn^{2+} into the $Cu_{1.81}S$ core.

The geometric barrier of CE can be overcome by elevating the reaction temperature to 155 °C. As shown in Fig. 3f–j and S12b,†

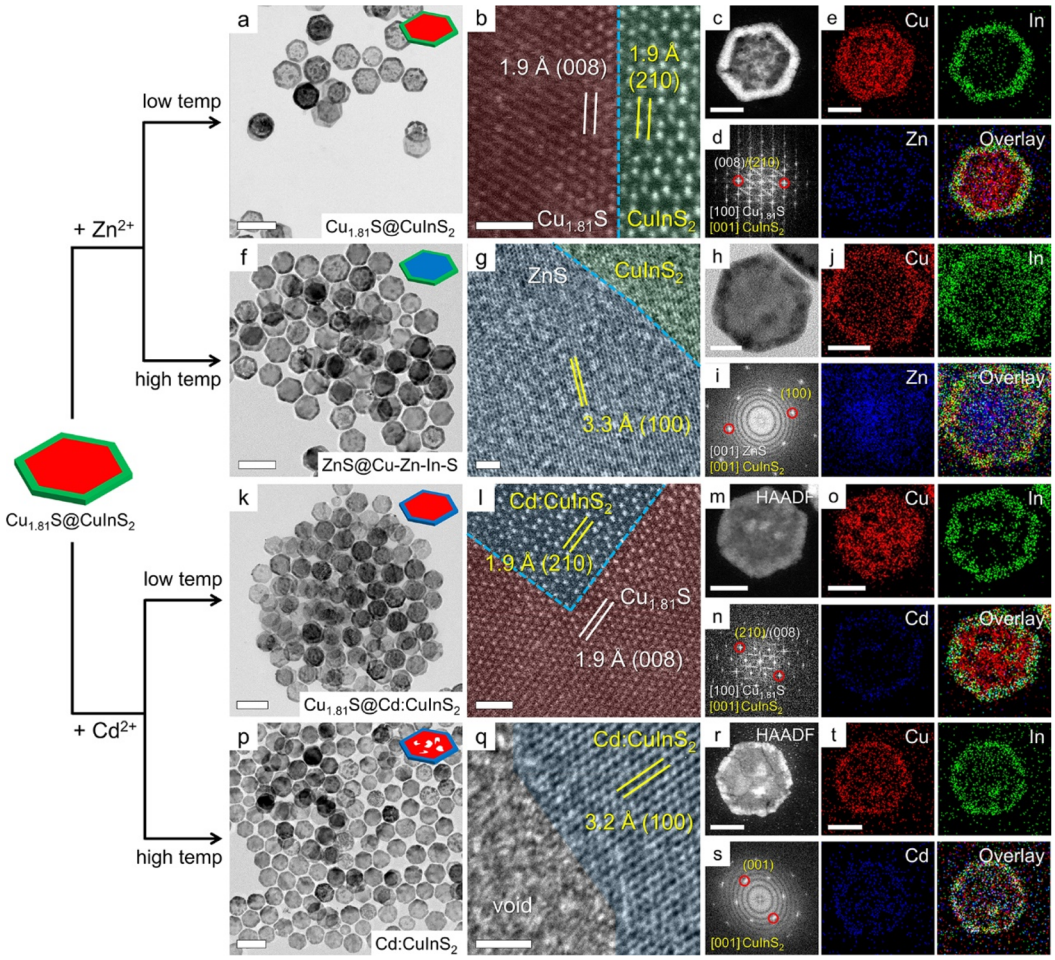

Fig. 3 CE reactions on $Cu_{1.81}S@CuInS_2$ core@shell heterostructures using Zn and Cd at low and high reaction temperatures. (a) TEM, (b) HRTEM, and (c) HAADF images, (d) FFT pattern, and (e) corresponding elemental maps of the CE reaction product obtained through Zn exchange at 55 °C. (f) TEM, (g) HRTEM, and (h) HAADF images, (i) FFT pattern, and (j) corresponding elemental maps of the CE reaction product obtained through Zn exchange at 155 °C. (k) TEM, (l) HRTEM, and (m) HAADF images, (n) FFT pattern, and (o) corresponding elemental maps of the CE reaction product obtained through Cd exchange at 55 °C. (p) TEM, (q) HRTEM, and (r) HAADF images, (s) FFT pattern, and (t) corresponding elemental maps of the CE reaction product obtained through Cd exchange at 155 °C. Scale bars: (a, f, k and p) 200 nm; (b, g, l and q) 2 nm; (c, h, m and r) 50 nm.

the Zn signals became dominant at the center of the heterostructure nanoplate but were still less pronounced at its rim, forming $(CuIn)_{0.28}Zn_{0.72}S_2@(CuIn)_{0.94}Zn_{0.06}S_2$ heterostructures. Wurtzite $CuInS_2$ and ZnS share the same crystal structure with slightly different lattice parameters. The broad diffraction peaks of the product nanoplates fell between the standard $CuInS_2$ and ZnS patterns and split at higher angles, indicating the formation of distinct zinc-rich and zinc-poor wurtzite phases (Fig. S13†). The $Zn \rightarrow Cu_{1.81}S$ reaction has the lowest regioselectivity, allowing Zn^{2+} to enter the $Cu_{1.81}S$ domain through both basal and edge planes. At high reaction temperatures, the Zn^{2+} ions tended to displace Cu^{+} from the basal planes, as evidenced by the similar level of Zn incorporation on edges at both high and low temperatures. This can be explained by the fact that the basal planes have more available surface area for the CE reactions compared to the edges, following an $A_{basal} : A_{edge}$ ratio of $3a/2h$, where a and h are the edge length and the height of the nanoplates, respectively ($a \gg h$). The formation of the quaternary phase in the center of the nanoplates indicates that some marginal In^{3+} can diffuse into the center during the substitution of Cu by Zn. We note that the experimental evidence supports the regioselectivity of Zn^{2+} incorporation into either the $CuInS_2$ shell or the $Cu_{1.81}S$ core of the heterostructural template. The difference in Zn content between the shell and the core of the nanoplates provides valuable insights. Despite the less pronounced incorporation of Zn into the $CuInS_2$ edges, the absence of Zn signals at the center of the nanoplate indicates that the regioselectivity of Zn incorporation is genuine. The limited Zn content on the $CuInS_2$ shell can be attributed to the weak chemical driving force and narrow diffusion channels. Upon elevating the reaction temperature, a substantial increase in Zn content was observed at the nanoplate centers, while the level of Zn incorporation at the edges remained relatively consistent compared to lower reaction temperatures. These results indicate that, in addition to the DFT-predicted regioselectivity, factors such as geometric effects and reaction kinetics should also be taken into account.

Similar to the reaction of Zn^{2+}, STEM-EDS elemental maps of the Cd^{2+} exchange reveal that there was only 5.7% Cd^{2+} located on the edges of the nanoplates, while the central Cu signals were unchanged (Fig. 3n and S14a†). This is consistent with the DFT calculations, which indicate that the formation of the $(CuIn)_{1-y}Cd_yS_2$ shell is attributed to the energetically more favorable $Cd \rightarrow CuInS_2$ reaction compared to the $Cd \rightarrow Cu_{1.81}S$ reaction on the basal planes. Fig. S15† shows that the XRD pattern shifted to a lower angle by 0.23°, indicating minor incorporation of large Cd^{2+} ions into the $CuInS_2$ lattice. When the reaction temperature is elevated to 155 °C, the Cd signals were still sparsely distributed on the edges of the nanoplates, with $y = 8.9\%$ (Fig. 3t and S14b†), which is supported by the additional 0.24° peak shift towards a lower angle. The elemental maps showed negligible Cd signals at the core of the nanoplates, consistent with the DFT calculations, which suggest that Cd prefers to diffuse through the edges of the $Cu_{1.81}S$ nanoplates. Cd^{2+} ions only diffused into the $CuInS_2$ shell when there were no $Cu_{1.81}S$ edges exposed. In addition to the energy difference, we speculate that the large radius of Cd^{2+} ions is another key factor that distinguishes the regioselectivity of the $Cd \rightarrow Cu_{1.81}S$ reaction from the $Zn \rightarrow Cu_{1.81}S$ reaction. Voids were formed on the $Cu_{1.81}S$ core when reacting with Cd^{2+} at higher temperatures (Fig. 3p and q), because the Cd^{2+} ions were only allowed to diffuse into the lattice through the narrow edges while the Cu^+ ions in the $Cu_{1.81}S$ core escaped from the nanoplates through the more open basal planes in the presence of Cu-extracting TOP, thus causing etching of the cores.[25,37,38]

Regioselectivity of CE reactions on $Cu_{1.81}S$/CdS(ZnS) heterostructures

To further understand the regioselectivity and mechanism of CE reactions involving In^{3+}, we carried out CE reactions on $Cu_{1.81}S$/ZnS(CdS) heterostructures. When the $Cu_{1.81}S$/CdS heterostructures were treated with In^{3+}, the $Cu_{1.81}S$ core of the nanoplates underwent significant etching, as shown in Fig. 4a

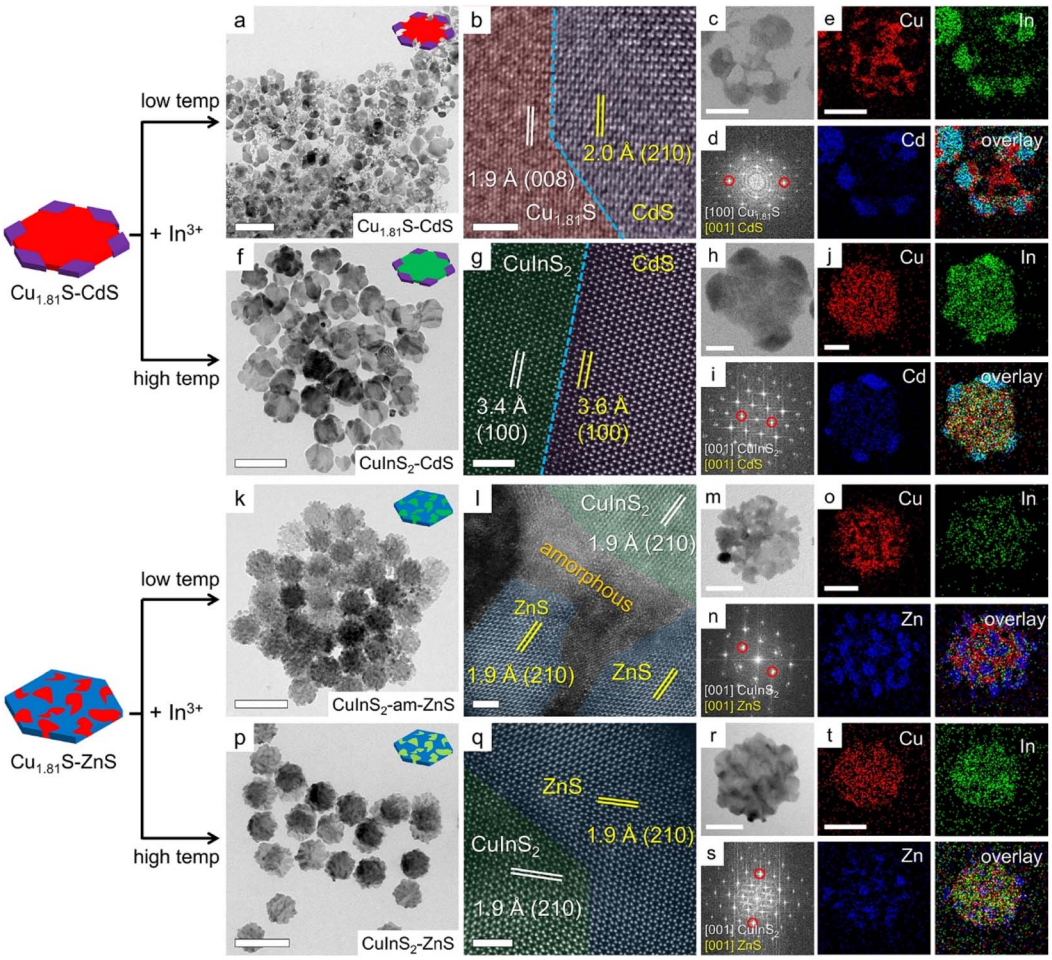

Fig. 4 CE reactions on $Cu_{1.81}S$/CdS and $Cu_{1.81}S$/ZnS heterostructures using In at low and high reaction temperatures. (a) TEM, (b) HRTEM, and (c) HAADF images, (d) FFT pattern, and (e) corresponding elemental maps of the CE reaction product obtained through In exchange on $Cu_{1.81}S$/CdS at 55 °C. (f) TEM, (g) HRTEM, and (h) HAADF images, (i) FFT pattern, and (j) corresponding elemental maps of the CE reaction product obtained through In exchange on $Cu_{1.81}S$/CdS at 155 °C. (k) TEM, (l) HRTEM, and (m) HAADF images, (n) FFT pattern, and (o) corresponding elemental maps of the CE reaction product obtained through In exchange on $Cu_{1.81}S$/ZnS at 55 °C. (p) TEM, (q) HRTEM, and (r) HAADF images, (s) FFT pattern, and (t) corresponding elemental maps of the CE reaction product obtained through In exchange on $Cu_{1.81}S$/ZnS at 155 °C. Scale bars: (a, f, k and p) 200 nm; (b, g, l and q) 2 nm; (c, h, m and r) 50 nm.

and c. STEM-EDS and elemental maps show that In^{3+} signals were not detected on either $Cu_{1.81}S$ or CdS domains (Fig. 4a and S10, S16a†). The negligible In^{3+} signal on CdS domains can be explained by the unfavored In → CdS reaction. The CdS domains served as a barrier that passivated the vertices of the template nanoplates. Therefore, the resulting nanoplates exhibited an XRD pattern close to that of CdS (Fig. S17†). This could also be elucidated by the nanoscale Kirkendall effect,[39–41] wherein the disparity between the inward diffusion rates of In^{3+} and the outward diffusion rates of Cu^{+} results in the formation of numerous defects and ultimately the collapse of the lattice structure. It is important to note that although the In^{3+} signals appeared visually strong, the actual In^{3+} content on the nanoplates was ≤0.5%. This was confirmed by performing CE reactions of In^{3+} on pure CdS nanoplates, where only a <2% In doping level was detected even at high reaction temperatures, further confirming the retarded In → CdS reaction (Fig. S18, and S19†). The discrepancy observed between the visual intensity of the signals in EDS elemental mapping and quantitative EDS results for In could potentially be attributed to the proximity of the EDS lines of Cd and In within the EDS spectra.

Surprisingly, no In incorporation into $Cu_{1.81}S$ was observed (Fig. 4a and S10†). The edge-favored In → $Cu_{1.81}S$ reaction was prohibited when the vertices were blocked. This observation indicates that, at a mild reaction driving force (55 °C), the CE reaction predominately occurs on the sterically opened vertices of the edges and then gradually spreads across the rest of the edges, consistent with the Cd → $Cu_{1.81}S$ reaction (Fig. S9†). The presence of the Cu-extracting TOP ligand and the absence of compensating cations lead to partial removal of the $Cu_{1.81}S$ domains.[37] A similar process was observed when incorporating hard acid Sn^{4+} into $Cu_{1.81}S$, where barely any Sn^{4+} can be detected but the $Cu_{1.81}S$ domains were completely expelled during CE reactions.[25] Because of the highly favorable In → $Cu_{1.81}S$ reaction, the blocking effect was partially screened at an elevated reaction temperature of 155 °C, producing $Cu_{1.85}In_{0.15}S_2$/CdS heterostructures with preserved hexagonal morphology (Fig. 4f). The XRD pattern (Fig. S17†), STEM-EDS results (Fig. S10†) and elemental maps (Fig. 4j and S16b†) also confirmed the coexistence of wurtzite of $CuInS_2$ and CdS.

The CE of In on $Cu_{1.81}S$/ZnS followed a similar mechanism compared to $Cu_{1.81}S$/CdS. As shown in Fig. 4k–o and S20a,† In^{3+} was selectively incorporated into $Cu_{1.81}S$ domains rather than ZnS domains, producing $Cu_{1.90}In_{0.10}S_2$/ZnS heterostructures. This selectivity became more pronounced at elevated reaction temperature, where the driving force for ion diffusion was sufficient, leading to the formation of nearly stoichiometric $Cu_{1.03}In_{0.97}S_2$/ZnS heterostructures (Fig. 4p–t and S20b†). The absence of In signals on ZnS domains was attributed to a strongly unfavored In → ZnS reaction (Fig. 1). Fig. 4l reveals the presence of amorphous regions at the heterointerfaces between $Cu_{1.90}In_{0.10}S_2$ and ZnS domains, which is supported by the peak broadening observed in the XRD pattern (Fig. S21†). The formation of these amorphous regions was attributed to the insufficient compensation of In^{3+} ions during the leaching out of Cu^{+} ions. This phenomenon is consistent with previous reports, indicating that ion removal and compensation mismatch during the CE process often lead to the formation of defective regions, local concaves, and lattice collapses.[39,40,42,43] At higher temperatures, In^{3+} ions could migrate into the $Cu_{1.81}S$ lattice more rapidly, resulting in the formation of a more crystalline and stoichiometric ternary phase, as supported by the XRD pattern (Fig. S21†).

Determinants of regioselectivity of CE reactions

Taking the above results together, we note that the most pronounced determinant influencing the regioselectivity of CE reactions on $Cu_{2-x}S$ and its heterostructures is the local electronic structures of the host lattice. DFT calculations provide accurate predictions of the CE outcomes by considering the local electronic structures that determine the acceptance of foreign cations. Specifically, CdS and $CuInS_2$ selectively grow on the edges and vertices of the nanoplates due to their high ΔE values, whereas the minimal ΔE value observed in the Zn → $Cu_{1.81}S$ reaction diminishes the selection, producing randomly distributed ZnS domains. The regioselectivity of the CE reaction on $Cu_{1.81}S$, coupled with the larger cation radius of Cd^{2+}, promotes the growth of CdS domains on the vertices of the nanoplates. Consequently, the subsequent In → $Cu_{1.81}S$ reaction is hindered as the In → CdS reaction is unfavored. The regio-blocking effect becomes more pronounced when the rim of the $Cu_{1.81}S$ nanoplates is fully encapsulated with the $CuInS_2$ shell. In contrast, In can be incorporated into the $Cu_{1.81}S$ domain in the $Cu_{1.81}S$/ZnS heterostructures owing to the randomly distributed ZnS domains. Despite the minor difference (≤0.2 eV) of $\Delta_r E_{basal}$ for four Cd/Zn → $Cu_{1.81}S$/$CuInS_2$ reactions, the CE reactions primarily occur on the rims of the nanoplates as the incoming cations preferentially diffuse through the energetically favored pathway of the $CuInS_2$ (010) planes, rather than $Cu_{1.81}S$ (100) planes. However, these regioselectivities become less dominant when elevating the reaction temperature, where the cation diffusion is strongly promoted. As a result, Zn ions begin to replace the Cu ions in the $Cu_{1.81}S$ domain of the core@shell structure. Cd ions exhibit a similar trend, but the large cation radius leads to sluggish reaction kinetics, producing voids on the nanoplates *via* a nanoscale Kirkendall effect. In contrast, the Kirkendall effect can be

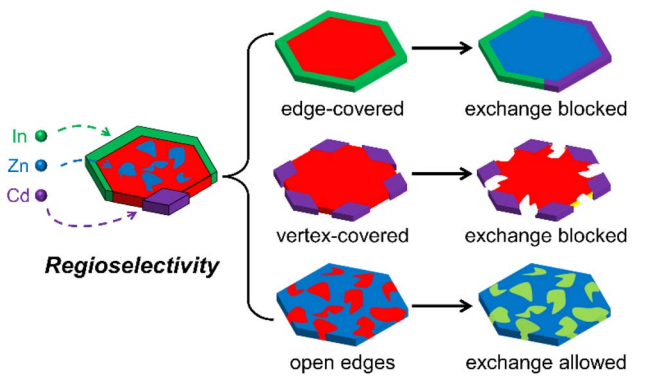

Scheme 1 Schematic illustration of the regioselectivity and blocking effect of CE reactions on a copper sulfide nanoplate.

avoided in In→$Cu_{1.81}S$/CdS(ZnS) reactions, where a high reaction driving force converts the $Cu_{1.81}S$ domain into nearly stoichiometric $CuInS_2$ without voids or defects. The overall regioselectivity and blocking effect of CE reactions are illustrated in Scheme 1.

Conclusions

In summary, we have investigated the determinants of the regioselectivity of CE reactions on $Cu_{2-x}S$ and its heterostructures by mutual corroboration between theoretical calculations and experimental results. Our findings revealed that the CE reactions exhibit a preference for occurring at the edges of the template nanoplates, owing to the presence of delocalized electrons in the incoming cations and sulfur ions. The subsequent CE reactions that could have occurred can now be suppressed by using passivated edges with unfavored CE reactions. The regioselectivity can be overridden when the reaction temperatures are elevated. By manipulating the local electronic environments, namely the metal–sulfur interaction in the lattice, we demonstrated the ability to create a diverse array of copper sulfide-based heterostructures. This work presents a promising approach for the development of novel copper sulfide-based heterostructures by leveraging these factors.

Data availability

The data supporting this article have been included as part of the ESI.†

Author contributions

Y. L. conceived and supervised this project. X. Q. performed most of the experiments. Y. L. and X. Q. conducted the detailed analysis of the experimental data. H. Z. performed the DFT calculations. T. G., F. Z., and Y. Z. contributed to the analysis and discussion of results. The manuscript was written through contributions of all authors. All authors have given approval to the final version of the manuscript.

Conflicts of interest

There are no conflicts to declare.

Acknowledgements

This study was financially supported by the National Key R&D Program of China (2024YFB3817400), the Science and Technology Commission of Shanghai Municipality (23ZR1405000 and 22YF1401900) and the National Natural Science Foundation of China (12174237 and 52301298).

Notes and references

1 T. Ling, M. Jaroniec and S. Z. Qiao, Recent Progress in Engineering the Atomic and Electronic Structure of Electrocatalysts via Cation Exchange Reactions, *Adv. Mater.*, 2020, **32**, e2001866.
2 W. He, I. Liberman, I. Rozenberg, R. Ifraemov and I. Hod, Electrochemically Driven Cation Exchange Enables the Rational Design of Active CO_2 Reduction Electrocatalysts, *Angew. Chem., Int. Ed.*, 2020, **59**, 8262–8269.
3 Q. Yuan, D. Liu, N. Zhang, W. Ye, H. Ju, L. Shi, R. Long, J. Zhu and Y. Xiong, Noble-Metal-Free Janus-like Structures by Cation Exchange for Z-Scheme Photocatalytic Water Splitting under Broadband Light Irradiation, *Angew. Chem., Int. Ed.*, 2017, **56**, 4206–4210.
4 Y. Chen, S. Zhao, X. Wang, Q. Peng, R. Lin, Y. Wang, R. Shen, X. Cao, L. Zhang, G. Zhou, J. Li, A. Xia and Y. Li, Synergetic Integration of $Cu_{1.94}S$-$Zn_xCd_{1-x}S$ Heteronanorods for Enhanced Visible-Light-Driven Photocatalytic Hydrogen Production, *J. Am. Chem. Soc.*, 2016, **138**, 4286–4289.
5 T. T. Zhuang, Y. Liu, Y. Li, Y. Zhao, L. Wu, J. Jiang and S. H. Yu, Integration of Semiconducting Sulfides for Full-Spectrum Solar Energy Absorption and Efficient Charge Separation, *Angew. Chem., Int. Ed.*, 2016, **55**, 6396–6400.
6 Z. Lian, M. Sakamoto, J. J. M. Vequizo, C. S. K. Ranasinghe, A. Yamakata, T. Nagai, K. Kimoto, Y. Kobayashi, N. Tamai and T. Teranishi, Plasmonic p–n Junction for Infrared Light to Chemical Energy Conversion, *J. Am. Chem. Soc.*, 2019, **141**, 2446–2450.
7 Z. Lian, M. Sakamoto, H. Matsunaga, J. J. M. Vequizo, A. Yamakata, M. Haruta, H. Kurata, W. Ota, T. Sato and T. Teranishi, Near Infrared Light Induced Plasmonic Hot Hole Transfer at a Nano-Heterointerface, *Nat. Commun.*, 2018, **9**, 2314.
8 H. Yang, F. Wang, H. Zhang, L. Guo, L. Hu, L. Wang, D. J. Xue and X. Xu, Solution Synthesis of Layered van der Waals (vdW) Ferromagnetic $CrGeTe_3$ Nanosheets from a Non-vdW Cr_2Te_3 Template, *J. Am. Chem. Soc.*, 2020, **142**, 4438–4444.
9 D. Tao, L. Ran, T. Li, Y. Cao and F. Xu, 3D Tunnel Copper Tetrathiovanadate Nanocube Cathode Achieving Ultrafast Magnesium Storage Reactions through a Charge Delocalization and Displacement Mechanism, *ACS Nano*, 2024, **18**, 28810–28821.
10 Z. Lian, M. Sakamoto, J. J. M. Vequizo, C. S. K. Ranasinghe, A. Yamakata, T. Nagai, K. Kimoto, Y. Kobayashi, N. Tamai and T. Teranishi, Plasmonic p–n Junction for Infrared Light to Chemical Energy Conversion, *J. Am. Chem. Soc.*, 2019, **141**, 2446–2450.
11 D. Xu, L. Zhai, Z. Mu, C. L. Tao, F. Ge, H. Zhang, M. Ding, F. Cheng and X. J. Wu, Versatile synthesis of nano-icosapods via cation exchange for effective photocatalytic conversion of biomass-relevant alcohols, *Chem. Sci.*, 2023, **14**, 10167–10175.
12 Y. Chen and L. Amirav, Shape tunability of copper nanocrystals deposited on nanorods, *Chem. Sci.*, 2023, **14**, 7512–7523.
13 J. L. Fenton, B. C. Steimle and R. E. Schaak, Tunable Intraparticle Frameworks for Creating Complex Heterostructured Nanoparticle Libraries, *Science*, 2018, **360**, 513–517.

14 B. Bai, C. Y. Zhao, M. Xu, J. B. Ma, Y. J. Du, H. L. Chen, J. J. Liu, J. Liu, H. P. Rong, W. X. Chen, Y. X. Weng, S. Brovelli and J. T. Zhang, Unique Cation Exchange in Nanocrystal Matrix via Surface Vacancy Engineering Overcoming Chemical Kinetic Energy Barriers, *Chem*, 2020, **6**, 3086–3099.

15 B. C. Steimle, J. L. Fenton and R. E. Schaak, Rational Construction of a Scalable Heterostructured Nanorod Megalibrary, *Science*, 2020, **367**, 418–424.

16 A. E. Powell, J. M. Hodges and R. E. Schaak, Preserving Both Anion and Cation Sublattice Features during a Nanocrystal Cation-Exchange Reaction: Synthesis of Metastable Wurtzite-Type CoS and MnS, *J. Am. Chem. Soc.*, 2016, **138**, 471–474.

17 Z. Li, M. Saruyama, T. Asaka, Y. Tatetsu and T. Teranishi, Determinants of crystal structure transformation of ionic nanocrystals in cation exchange reactions, *Science*, 2021, **373**, 332–337.

18 J. L. Fenton, B. C. Steimle and R. E. Schaak, Exploiting Crystallographic Regioselectivity To Engineer Asymmetric Three-Component Colloidal Nanoparticle Isomers Using Partial Cation Exchange Reactions, *J. Am. Chem. Soc.*, 2018, **140**, 6771–6775.

19 R. E. Schaak, B. C. Steimle and J. L. Fenton, Made-to-Order Heterostructured Nanoparticle Libraries, *Acc. Chem. Res.*, 2020, **53**, 2558–2568.

20 B. C. Steimle, A. M. Fagan, A. G. Butterfield, R. W. Lord, C. R. McCormick, G. A. Di Domizio and R. E. Schaak, Experimental Insights into Partial Cation Exchange Reactions for Synthesizing Heterostructured Metal Sulfide Nanocrystals, *Chem. Mater.*, 2020, **32**, 5461–5482.

21 C. R. McCormick, R. R. Katzbaer, B. C. Steimle and R. E. Schaak, Combinatorial Cation Exchange for the Discovery and Rational Synthesis of Heterostructured Nanorods, *Nat. Synth.*, 2023, **2**, 152–161.

22 E. A. Eikey, X. Y. Gan, D. C. Kaseman, C. G. E. Murphey, S. E. Crawford, K. A. Johnston, S. Yazdi and J. E. Millstone, Efficient Control of Atom Arrangement in Ternary Metal Chalcogenide Nanoparticles Using Precursor Oxidation State, *Chem. Mater.*, 2020, **32**, 1322–1331.

23 X. Y. Gan, R. Sen and J. E. Millstone, Connecting Cation Exchange and Metal Deposition Outcomes via Hume–Rothery-Like Design Rules Using Copper Selenide Nanoparticles, *J. Am. Chem. Soc.*, 2021, **143**, 8137–8144.

24 S. Lee, S. Baek, J. P. Park, J. H. Park, D. Y. Hwang, S. K. Kwak and S. W. Kim, Transformation from $Cu_{2-x}S$ Nanodisks to $Cu_{2-x}S$@$CuInS_2$ Heteronanodisks via Cation Exchange, *Chem. Mater.*, 2016, **28**, 3337–3344.

25 Y. Liu, M. Liu, D. Yin, L. Qiao, Z. Fu and M. T. Swihart, Selective Cation Incorporation into Copper Sulfide Based Nanoheterostructures, *ACS Nano*, 2018, **12**, 7803–7811.

26 L. De Trizio, F. De Donato, A. Casu, A. Genovese, A. Falqui, M. Povia and L. Manna, Tailoring Cu^+ for Ga^{3+} Cation Exchange in $Cu_{2-x}S$ and $CuInS_2$ Nanocrystals by Controlling the Ga Precursor Chemistry, *ACS Nano*, 2019, **13**, 12880–12893.

27 Y. Liu, D. Yin and M. T. Swihart, Valence Selectivity of Cation Incorporation into Covellite CuS Nanoplatelets, *Chem. Mater.*, 2018, **30**, 1399–1407.

28 W. van der Stam, A. C. Berends, F. T. Rabouw, T. Willhammar, X. Ke, J. D. Meeldijk, S. Bals and C. de Mello Donega, Luminescent $CuInS_2$ Quantum Dots by Partial Cation Exchange in $Cu_{2-x}S$ Nanocrystals, *Chem. Mater.*, 2015, **27**, 621–628.

29 S. Paul, B. Dalal, R. Jana, A. Shit, A. Datta and S. K. De, Enhanced Photophysical Properties of Bi_2S_3/$AgBiS_2$ Nanoheterostructures Synthesized via Ag(I) Cation Exchange-Mediated Transformation of Binary Bi_2S_3, *J. Phys. Chem. C*, 2020, **124**, 12824–12833.

30 K. Koumpouras and J. A. Larsson, Distinguishing between chemical bonding and physical binding using electron localization function (ELF), *J. Phys. Condens. Matter*, 2020, **32**, 315502.

31 A. Scemama, P. Chaquin and M. Caffarel, Electron pair localization function: a practical tool to visualize electron localization in molecules from quantum Monte Carlo data, *J. Chem. Phys.*, 2004, **121**, 1725–1735.

32 E. R. A. Beronio, I. R. Colambo and A. A. B. Padama, The effects of substitutional doping on Cu vacancy formation in Cu_2O(111): a density functional theory study, *Phys. Chem. Chem. Phys.*, 2021, **23**, 8800–8808.

33 J. X. Xia, R. L. Zhang, J. S. Luo, H. Yang, H. Y. Shu, H. A. Malik, Z. Q. Wan, Y. Shi, K. L. Han, R. L. Wang, X. J. Yao and C. Y. Jia, Dipole Evoked Hole-Transporting Material p-Doping by Utilizing Organic Salt for Perovskite Solar Cells, *Nano Energy*, 2021, **85**, 106018.

34 L. P. Chi, Z. Z. Niu, X. L. Zhang, P. P. Yang, J. Liao, F. Y. Gao, Z. Z. Wu, K. B. Tang and M. R. Gao, Stabilizing indium sulfide for CO_2 electroreduction to formate at high rate by zinc incorporation, *Nat. Commun.*, 2021, **12**, 5835.

35 L. De Trizio, H. Li, A. Casu, A. Genovese, A. Sathya, G. C. Messina and L. Manna, Sn Cation Valency Dependence in Cation Exchange Reactions Involving $Cu_{2-x}Se$ Nanocrystals, *J. Am. Chem. Soc.*, 2014, **136**, 16277–16284.

36 R. D. Shannon, Revised Effective Ionic Radii and Systematic Studies of Interatomic Distances in Halides and Chalcogenides, *Acta Crystallogr.*, 1976, **32**, 751–767.

37 A. Nelson, D. H. Ha and R. D. Robinson, Selective Etching of Copper Sulfide Nanoparticles and Heterostructures through Sulfur Abstraction: Phase Transformations and Optical Properties, *Chem. Mater.*, 2016, **28**, 8530–8541.

38 H. L. Young, C. R. McCormick, A. G. Butterfield, E. D. Gomez and R. E. Schaak, Postsynthetic Thiol-Induced Reshaping of Copper Sulfide Nanoparticles, *Chem. Mater.*, 2022, **34**, 11014–11025.

39 Y. Liu, M. Liu and M. T. Swihart, Shape Evolution of Biconcave Djurleite $Cu_{1.94}S$ Nanoplatelets Produced from $CuInS_2$ Nanoplatelets by Cation Exchange, *J. Am. Chem. Soc.*, 2017, **139**, 18598–18606.

40 L. Mu, F. Wang, B. Sadtler, R. A. Loomis and W. E. Buhro, Influence of the Nanoscale Kirkendall Effect on the Morphology of Copper Indium Disulfide Nanoplatelets Synthesized by Ion Exchange, *ACS Nano*, 2015, **9**, 7419–7428.

41 Y. Hong, T. Kim, J. Jo, B. Kim, H. Jin, H. Baik and K. Lee, Highly Crystalline Hollow Toroidal Copper Phosphosulfide via Anion Exchange: A Versatile Cation Exchange Nanoplatform, *ACS Nano*, 2020, **14**, 11205–11214.

42 W. S. Wang, M. Dahl and Y. D. Yin, Hollow Nanocrystals through the Nanoscale Kirkendall Effect, *Chem. Mater.*, 2013, **25**, 1179–1189.

43 Y. Li, J. Liu, X. Li, X. Wan, R. Pan, H. Rong, J. Liu, W. Chen and J. Zhang, Evolution of Hollow $CuInS_2$ Nanododecahedrons via Kirkendall Effect Driven by Cation Exchange for Efficient Solar Water Splitting, *ACS Appl. Mater. Interfaces*, 2019, **11**, 27170–27177.